Development of Two-Color Laser Imaging Interferometer Using CO_2 Laser and Quantum Cascade Laser in the Large Helical Device

Toshiki KINOSHITA, Kenji TANAKA[1)], Yuki TAKEMURA[1,2)], Shota TAKESHIDA[a)] and Hikona SAKAI

Interdisciplinary Graduate School of Engineering Sciences, Kyushu University, Kasuga, Fukuoka 816-8580, Japan
[1)]*National Institute for Fusion Science, National Institutes of Natural Sciences, Toki, Gifu 509-5292, Japan*
[2)]*The Graduate University for Advanced Studies, SOKENDAI, Toki, Gifu 509-5292, Japan*

(Received 6 September 2022 / Accepted 18 October 2022)

CO_2 laser interferometers are a promising option for high-density plasma measurements. However, in low- and middle-density measurements, noise due to mechanical vibrations is a serious problem. To remove this noise, we developed a two-color laser imaging interferometer using a CO_2 laser and quantum cascade (QC) laser, called the CO_2/QC laser imaging interferometer, through benchtop experiments and installed it in the Large Helical Device (LHD). Benchtop experiments provided optical design guidelines for the CO_2/QC laser imaging interferometer to minimize the influence of the unstable output wavelength of the QC laser. The optical system in LHD was designed according to this guideline, and the vibration noise was successfully reduced to 2.80×10^{18} m^{-3}. We also demonstrate measurement examples of hollowed and peaked electron density profiles evaluated using Abel inversion and macro-scale instability. This is the first study to present the measurement results of high-temperature plasma using a CO_2/QC two-color laser interferometer. The study outcomes provide important insights for the development of two-color laser interferometers in future fusion devices.

Keywords: plasma diagnostics, interferometer, CO_2 laser, quantum cascade laser, LHD

DOI: 10.1585/pfr.17.1402107

1. Introduction

Interferometers are powerful diagnostic tools for electron density measurements in high-temperature plasmas. The measured electron density is used to monitor the plasma electron density and as a source for density feedback control. In addition, the interferometer provides essential information for physical investigations. For instance, flux surface-averaged radial density profiles evaluated by the Abel inversion of multichannel line-integrated density were used for transport analyses and stability calculations [1, 2]. In addition, the fine temporal evolution of electron density can be used to investigate macro- and micro-instabilities [3, 4]. In the interferometer, the electron density is evaluated from the interference between electromagnetic waves passing through the plasma and those passing outside it. The phase velocity of an electromagnetic wave in the plasma changes depending on the plasma's refractive index, resulting in a phase shift owing to the interference. This is a simple function of the electron density and wavelength of a light source [5]. Thus, the electron density can be precisely evaluated for a given wavelength of the light source without calibration, which is in strong contrast to Thomson scattering electron density measurements, which require calibration experiments [6].

In this study, we developed a two-color laser imaging interferometer using a CO_2 laser and a quantum cascade (QC) laser, called the CO_2/QC laser imaging interferometer, for stable and reliable electron density measurements with fine time and spatial resolutions in the Large Helical Device (LHD). The remainder of this paper is organized as follows: In Sec. 2, the motivation for the development of the CO_2 laser interferometer for LHD is introduced, and mechanical vibration compensation using a two-color laser interferometer is presented. The results of benchtop experiments using the new detection method for the two-color scheme are presented in Sec. 3. Section 4 explains the optical design of the CO_2/QC laser imaging interferometer in LHD. Section 5 reports the measurement results of LHD. Finally, the summary and discussion are presented in Secs. 6 and 7, respectively.

2. Background and Motivation

2.1 CO_2 laser interferometer

In LHD, most plasma experiments are performed at an electron density of $n_e = 1 \times 10^{19}$ - 1×10^{21} m^{-3}. This density regime is typical for current tokamak and stellarator/heliotron devices. To measure the electron density in

author's e-mail: t.kinoshita@triam.kyushu-u.ac.jp
[a)] Presently with Chubu Electric Power Co., Inc.

LHD, a single-channel millimeter-wave (λ = 1 mm, 2 mm) interferometer [7] and a 13-channel CO_2 laser-pumped CH3OH far-infrared (FIR) laser (λ = 119 μm) interferometer [8–10] have been used since the beginning of the LHD project in 1998. The details of these interferometer systems are summarized in [11]. The measurable density of the millimeter-wave interferometer is limited to less than $n_e \sim 3 \times 10^{19}\,\mathrm{m}^{-3}$ because of the large divergence of the beam passing through the plasma center, which reduces the signal intensity. In addition, the FIR interferometer is ineffective in high-density plasma for pellet injection, radiation collapse, and plasma detachment, where the average density exceeds $1 \times 10^{20}\,\mathrm{m}^{-3}$ [12] because of the signal reduction caused by beam refraction, resulting in a phase jump [13]. Beam refraction effects are proportional to the square of the laser's wavelength [5]. Thus, the use of a shorter wavelength is a promising option for high-density measurements. Therefore, we selected a CO_2 laser (λ = 10.6 μm) as the light source for the high-density plasma measurements. The availability of a reliable laser and sensitive detector array is another reason for the selection of the 10.6 μm wavelength. Notably, the availability of a sensitive multichannel detector array is advantageous for realizing a larger number of channels. In a conventional interferometer, one beam corresponds to a measurement channel such as the FIR laser interferometer in LHD. However, an interferometer that uses sheet beams enables a larger number of channels using a multichannel detector array. Imaging optics were employed in LHD for multichannel systems using sheet beams [12, 14] after performing benchtop experiments [15]. The use of short-wavelength lasers presents a serious problem in that the phase shift owing to mechanical vibrations cannot be ignored. Therefore, the phase shift ϕ of the interference consists of phase shifts owing to the line-integrated electron density n_eL (n_e: electron density, L: plasma size) and those owing to the mechanical vibration x. The total phase shift is given by the following equation:

$$\phi = \frac{e^2}{4c^2\pi\varepsilon_0 m_e} n_e L\lambda + \frac{2\pi x}{\lambda}, \tag{1}$$

where e, c, ε_0, and m_e are the electric charge, speed of light, electric constant, and electron mass, respectively. The first term in Eq. (1), which is the phase shift due to electron density, is proportional to the wavelength. The second term, which is the phase shift due to mechanical vibration, is inversely proportional to the wavelength. If the signal-to-noise ratio is defined by the phase shift due to electron density, as opposed to that due to vibration, the signal-to-noise ratio is proportional to the square of the wavelength, indicating that a longer wavelength induces a considerably lower contribution from mechanical vibration. In LHD, the second term is negligible in most experiments on the wavelengths of the FIR and millimeter regions. However, while using a 10.6 μm wavelength enables high-density measurements, the exclusion of mechanical vibrations is necessary because the second term is not negligible.

2.2 Concept of the two-color laser interferometer

The phase shift owing to mechanical vibration can be removed using a second coaxial interferometer using a different wavelength. This system is called a two-color laser interferometer, which has already been installed in several toroidal devices, such as DIII-D [16], Alcator C-mod [17], JT-60U [18], and LHD [14]. In addition, it was selected for ITER [19] and JT-60SA [20]. A schematic of the two-color laser interferometer is shown in Fig. 1. The beam passing through the plasma is called the probe beam and that passing outside the plasma is called the local beam. In Fig. 1, the solid and dashed lines from beam splitters (BSs) 1 and 2 to BSs 3 and 4 indicate the probe and local beams, respectively. The beams of the first and second lasers are indicated by red and blue lines, respectively. For heterodyne detection, an acousto-optic modulator (AOM) causes a small frequency shift, and the first and second beams are aligned coaxially using a beam combiner (BC). The probe and local beams are then divided into two parts: one for plasma measurements and the other for a reference. After the probe beam passes through the plasma, the probe beam interferes with the local beam and is detected as a heterodyne beat signal. Detector 1p and 2p represent the detectors that detect the signals of the first and second in-

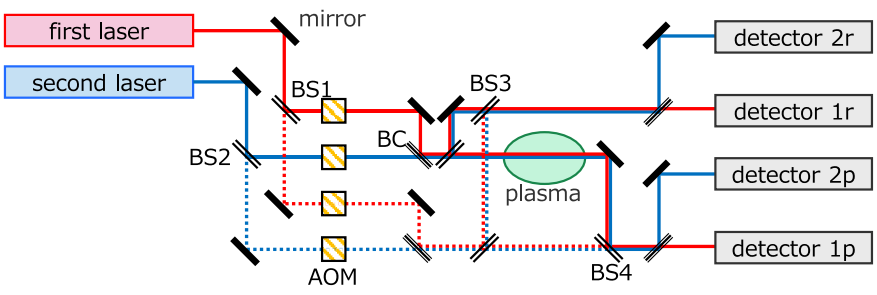

Fig. 1 Schematic diagram of the two-color interferometer. Red and blue represent the first and second laser beams, respectively. Solid and dashed lines indicate the probe and local beams, respectively.

terferometers that measure the plasma, respectively, and 1r and 2r represent the reference first and second interferometers, respectively. To compensate for mechanical vibrations, the wavelengths of the first and second lasers, λ_1 and λ_2, are substituted into Eq. (1), and the simultaneous equations are solved for n_eL and x. The solutions obtained were as follows:

$$n_eL = \frac{1}{A}B(\phi_1 - \phi_2\frac{\lambda_2}{\lambda_1}), \tag{2}$$

$$x = \frac{1}{2\pi}(\phi_1\lambda_2 - \phi_1\lambda_1)\frac{\lambda_1\lambda_2}{{\lambda_2}^2 - {\lambda_1}^1}, \tag{3}$$

$$A = \frac{e^2}{4c^2\pi\varepsilon_0 m_e} = 2\pi \times 4.49\times10^{-16}, \tag{4}$$

$$B = \frac{\lambda_1}{\lambda_1^2 - \lambda_2^2}. \tag{5}$$

Here, ϕ_1 is the phase shift of the first interferometer obtained from the phase difference between detectors 1p and 1r. Similarly, ϕ_2 is the phase shift of the second interferometer obtained from the phase difference between detectors 2p and 2r. Equations (2) and (3) are the line-integrated density n_eL and mechanical vibration x, respectively. However, in practice, the compensation for mechanical vibration is not perfect, and there are residual uncompensated components, as shown in the parentheses of Eq. (2). The following mechanical vibration cannot be compensated for using a two-color scheme:

(A) Mechanical vibration before combining and after separating the first and second laser.
(B) Mechanical vibration perpendicular to the beam axis.

Effect (A) can be minimized by decreasing the path length before combining and after separating the beams. However, the space requirement of the optical system restricts the minimization. Effect (B) is shown in Fig. 2. For Fig. 2 (a), perpendicular vibrations do not affect the phase shift if the wavefronts of the probe and local beam of the first and second laser are plane. For Fig. 2 (b), perpendicular vibrations can be compensated for if the wavefront curvatures are identical for the first and second lasers. This is because the perpendicular vibrations induce identical wavefront motion for the two lasers and identical wavefront parallel motion. As shown in Fig. 2 (c), perpendicular vibrations cannot be compensated for if wavefront curvatures are different in the first and second lasers. Furthermore, as shown in Fig. 2 (d), perpendicular vibrations cannot be compensated for if the wavefront is different for the two lasers. Perpendicular vibrations induce different parallel movements in the wavefront of the two lasers. The effects of the different wavefront curvatures shown in Fig. 2 (c) can be reduced using collimated beams. However, the effects of different wavefronts are sometimes difficult to reduce, as shown in Fig. 2 (d). Such wavefront differences are caused by the interference between multiple reflections of the front and back of the beam splitters and windows and the roughness of the optic surface. Generally, these effects are more significant at shorter wavelengths. In addition, a shorter wavelength makes beam mixing difficult and the beat signal unstable. Therefore, for the perpendicular vibration effect, two closer wavelengths are preferable, and for beat signal stability, a longer wavelength is preferable. However, closer wavelengths increase B in Eqs. (2) and (5) and enhance the effect of the uncompensated residual components in the parentheses of Eq. (2) on the phase shift. In addition, a short wavelength generally causes an unstable interference signal because of wavefront distortion, as shown by the blue line in Fig. 2 (d). The following are the guidelines for selecting these two wavelengths:

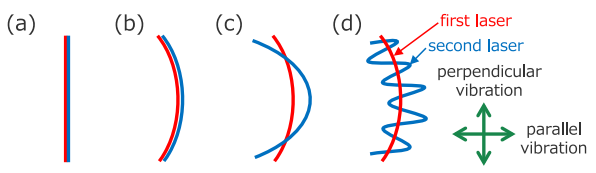

Fig. 2 Wavefront of the two-color laser interferometer.

(1) The wavelength of the first laser must be selected considering the target density and spatial resolution.
(2) The wavelength of the second laser must be closer to the first to reduce the effects of perpendicular vibration.
(3) The wavelength of the second laser must be farther from that of the first laser to reduce B.
(4) Both laser wavelengths must not be too short for the stable interference beat signal.

Based on these guidelines, we selected a CO_2 laser (λ = 10.6 μm) as the first laser. Our initial choice for the second laser a Nd:YAG laser (λ = 1.06 μm) [12, 14]. However, the beat signal of the YAG laser interferometer is unstable impeding stable operation. This is owing to wavefront distortion, which may be caused by multiple reflections from the BS, windows, and roughness of the optics. Thus, we selected a laser with a wavelength that was closer to that of the first laser. A closer wavelength reduces the residual vibration owing to the reduced effect of the perpendicular vibration; however, the contribution of the residual vibration is enhanced. In addition, considering the availability of a stable laser, we selected a wavelength of approximately ~5 μm for the second interferometer and QC laser.

3. Benchtop Experiment Using the New Detection System

As discussed in the previous section, the QC laser was selected as the light source for the second interferometer because the wavelength must be approximately 5 μm. The QC laser is a new type of semiconductor laser that utilizes population inversion between the subbands of the quantum well. Commercial products of 4 - 10 μm have become available in the last decade. In this wavelength re-

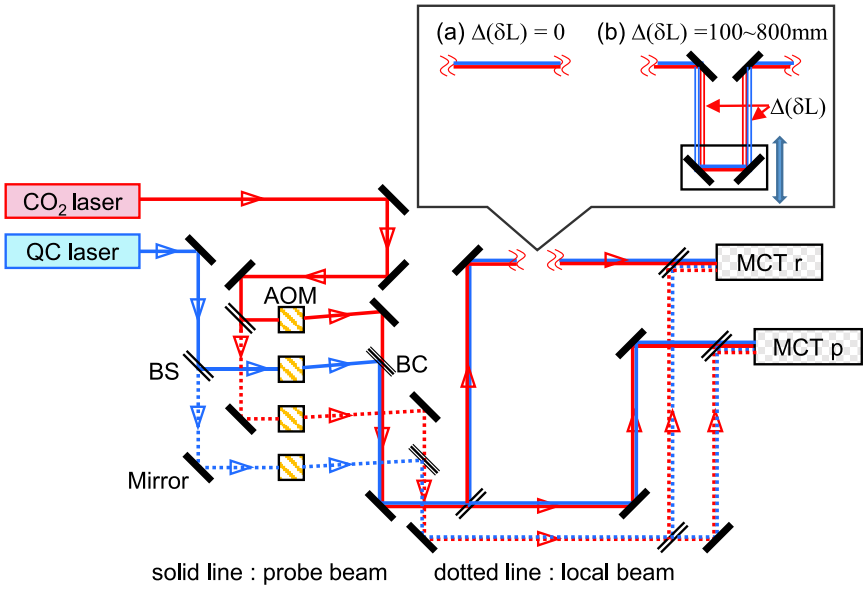

Fig. 3 Layout of the benchtop experiment of the CO_2/QC laser interferometer. Red and blue lines indicate the paths of the CO_2 laser and QC laser, respectively. Solid and dotted lines after the first BSs indicate the probe and local beams, respectively.

gion, the CO laser is a possible alternative to a QC laser. The cavity length of the CO laser is approximately ~1 m, whereas that of the QC laser is approximately ~0.15 m for an output power of 1 W. Therefore, the QC laser is much more compact than the CO laser, allowing for shorter path lengths before combination with the CO_2 laser, resulting in lower uncompensated vibration components. The QC laser has been planned for use in ITER's two-color interferometer [19]; however, there are no examples of measuring the electron density in high-temperature plasma. Therefore, our study provides valuable information for next-generation interferometers. Before installing LHD, benchtop experiments were conducted to confirm the technical feasibility of the CO_2/QC laser interferometer.

Figure 3 shows the optical system of the CO_2/QC laser interferometer used in the benchtop experiment. Because the feasibility of the imaging interferometer using wide-sheet beams has already been confirmed in previous studies [15], the vibration compensation was tested with a single channel. For bench testing, a CO_2 laser (MPB Technologies, model GN-802-GES) with an output power of 8 W was used. The wavelength was fixed at 10.6 μm by the grating and cavity length was feedback-controlled to stabilize the wavelength and power. A QC laser (Hamamatsu Photonics, model L12005-1900H-C) with an output power of 50 mW was used. The wavelength was controlled using a Peltier thermoelectric cooler driver (model C11330-01) and fixed at 5.26 μm. These are water-cooling lasers that suppress mechanical vibrations. The CO_2/QC laser interferometer uses a heterodyne detection technique. To obtain a heterodyne beat frequency $\omega_b/2\pi$ of 190 kHz for the CO_2 laser and 100 kHz for the QC laser, the frequency shift $\omega_{IF}/2\pi$ presented in Table 1 was applied to

Table 1 Intermediate frequencies given by AOM and obtained beat frequencies.

laser	beam	$\omega_{IF}/2\pi$ (MHz)	$\omega_b/2\pi$ (kHz)
CO_2 laser	local	40	190
	probe	40.19	
QC laser	local	40	100
	probe	40.1	

the local and probe beams using AOM. In conventional two-color interferometers [14], the combined beams of the first and second lasers are separated and detected by a detector corresponding to each wavelength, as shown in Fig. 1. In contrast, our interferometer system uses a single detector for both wavelengths. In this system, the detection optics are simpler than conventional two-color interferometers. In addition, the effects of vibration were lower because the beams of the two wavelengths were not separated for detection. A similar detection system has been proposed in a two-color interferometer using the far-infrared region (λ = 57.2 and 47.6 μm) for future fusion devices [21]. The detector was a liquid nitrogen-cooled photoconductive mercury cadmium tellurium (MCT) detector produced by the Infrared Systems Development Corporation. Figure 4 (a) shows the sensitivity spectrum of the MCT detector, considering the transmissivity of the detector window made of zinc selenide (ZnSe). This broad sensitivity enables the simultaneous detection of a CO_2 laser (λ = 10.6 μm) and QC laser (λ = 5.26 μm). Therefore, as illustrated in Fig. 4 (b), heterodyne beat signals of 190 and 100 kHz were obtained for the CO_2 laser and QC laser.

Sidebands caused by noise from the RF signal input to the AOM were observed at approximately 190 kHz; however, these sidebands were approximately two orders of magnitude smaller than the main signal and did not have a significant effect on the measurement. The CO_2 laser had a higher laser output power than the QC laser. In addition, the sensitivity of the QC laser is weaker than that of the CO_2 laser. Thus, to achieve the same beat signal amplitude, we adjusted the input RF power to the AOM and reduced the first-order diffracted light intensity of the CO_2 laser. In the benchtop experiment, the path length from the laser aperture to the detector was ~ 4 m, and the beam width ($1/e^2$ width) was ~20 mm at the detector.

The coherent length and stability of the wavelength are essential for an interferometer-laser source. However, these quantities are not yet clearly understood. In benchtop experiments, coherence and wavelength stability were also investigated for the CO_2 and QC lasers.

In Fig. 3, the path length of the probe beams entering the MCTr and MCTp after passing through the BC are defined as L_{rp} and L_{pp}, respectively, and those entering the MCTr and MCTp without passing through the BC are defined as L_{rl} and L_{pl}, respectively. The path length differences between the probe and local beams entering MCTr and MCTp are δL_r (= $L_{rp} - L_{rl}$) and δL_p (= $L_{pp} - L_{pl}$), respectively. The difference between δL_r and δL_p is denoted by $\Delta(\delta L)$. If all path lengths are identical, that is, $L_{rp} = L_{rl} = L_{pp} = L_{pl}$, coherence, stability coherence, and stability are insignificant. However, it is difficult to obtain such a layout using an experimental device. To obtain a heterodyne beat signal, the path difference between the probe and local beams, δL_p and δL_r, must be shorter than the coherent length. In the benchtop experiments, initially, δL_r and δL_p were set to 116 mm, and $\Delta(\delta L)$ was set to zero, as shown in Fig. 3 (a). Subsequently, $\Delta(\delta L)$ was scanned from 100 to 800 mm, as shown in Fig. 3 (b). Taking the mechanical vibration as Δx_r and Δx_p) for MCTr and MCTp, respectively, the heterodyne beat signals are given by the following equation:

$$\mathrm{MCTr} \propto \cos 2\pi \left(f_{b,i} t + \frac{\delta L_r + \Delta x_r}{\lambda_i} \right), \tag{6}$$

$$\mathrm{MCTp} \propto \cos 2\pi \left(f_{b,i} t + \frac{\delta L_p + \Delta(\delta L) + \Delta x_p}{\lambda_i} \right). \tag{7}$$

Here, the subscript i indicates the type of interferometer light source. The interferometer measures the phase difference ϕ between Eq. (6) and (7) and is given by the following equation for $\delta L_r = \delta L_p$

$$\phi = 2\pi \frac{\Delta(\delta L) + \Delta x_p - \Delta x_r}{\lambda_i}, \tag{8}$$

Here, Δx_p and Δx_r vary with time, and λ_i also varies with time for the unstable laser. Equation (8) indicates that, to minimize the effect of the unstable wavelength, the gap in the path difference between the probe and local path lengths of the two detectors, $\Delta(\delta L)$ should be reduced. Otherwise, a phase shift appears because of a change in the laser wavelength.

Figure 5 shows the time evolution of the phase change at two $\Delta(\delta L)$ values, (a) $\Delta(\delta L)$ = 800 mm and (b) $\Delta(\delta L)$ = 0 mm, and (c) an expanded view of $\Delta(\delta L)$ = 0 mm at t =

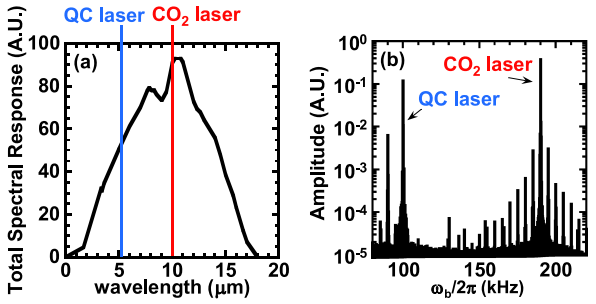

Fig. 4 (a) Total spectral response considered by the MCT detector including window transmission and (b) amplitude spectrum of the heterodyne beat signal measured by the MCT detector.

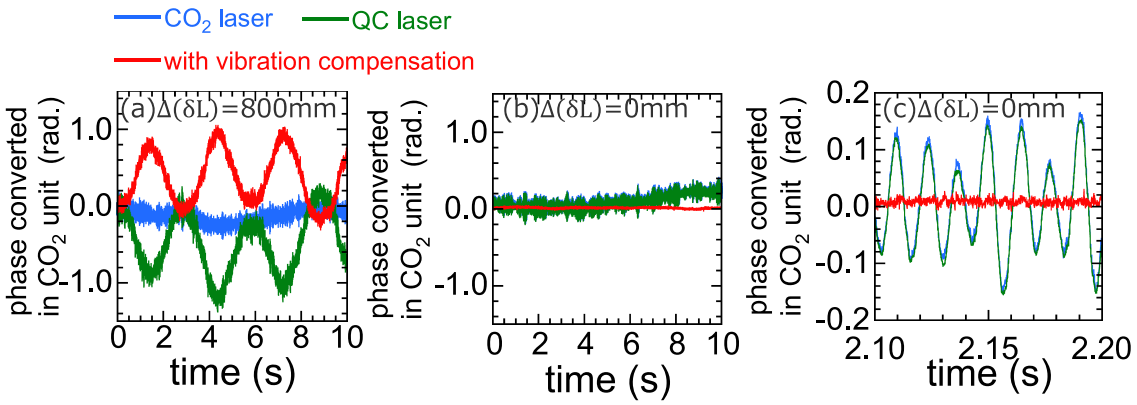

Fig. 5 Time evolution of the phase shift at (a) $\Delta(\delta L)$ = 800 mm, (b) $\Delta(\delta L)$ = 0 mm and (c) expanded view of ΔL = 0 mm at t = 2.1~2.2 s. δL_p and δL_r is fixed to be 116 mm.

2.1 - 2.2 s. δL_r and δL_p are fixed at 116 mm. The heterodyne beat signal amplitudes of the CO_2 and QC lasers measured at MCTr were almost comparable for $\Delta(\delta L) = 0$ and 800 mm. These results indicate that the coherent lengths of both lasers are considerably longer than the path difference of 916 mm and are sufficiently long for the interferometer. The time evolution of the phase shift between MCTr and MCTp was evaluated using the digital phase demodulation technique, which is a time–frequency analysis [13, 14, 22], where the units of the phase shift are converted values in the CO_2 laser wavelength. In Fig. 5, the blue, green, and red lines indicate the phase shift of the CO_2 and QC lasers and the subtracted phase shift of the QC laser from that of the CO_2 laser, respectively. The phase shift of the CO_2 laser fluctuates within ±0.3 rad. at several tens of hertz for both $\Delta(\delta L) = 800$ mm and $\Delta(\delta L) = 0$ mm. Because it is independent of $\Delta(\delta L)$, the observed phase shift is not due to the unstable output wavelength, but due to mechanical vibration. In contrast, the QC laser demonstrated large periodic fluctuations, and the peak-to-peak value was approximately 1.5 rad at ~0.3 Hz for $\Delta(\delta L) = 800$ mm, as shown in Fig. 5 (a). However, the fluctuations disappear at $\Delta(\delta L) = 0$ mm, as shown in Fig. 5 (b). Figure 5 (c) shows that the phase fluctuation of the CO_2 and QC lasers match well at $\Delta(\delta L) = 0$ mm. Subsequently, the phase shift due to mechanical vibrations was reduced to 0.04 rad, as indicated by the red line.

Figure 6 shows the $\Delta(\delta L)$ dependence of the peak-to-peak phase-shift amplitude for 10 s. The phase shift of the CO_2 laser is almost constant, regardless of $\Delta(\delta L)$. This result indicates that the output wavelength of the CO_2 laser is stable over time. In contrast, the phase shift of the QC laser increases with an increase in $\Delta(\delta L)$. This result indicates that the wavelength of the QC laser changed with time. Consequently, the phase shift after vibration compensation decreased with a decrease in $\Delta(\delta L)$; however, it was not zero. The frequency of the uncompensated components was several tens of hertz, which was close to the vibration frequency. Thus, uncompensation is likely due to the uncompensated vibration caused by the different wavefronts of the CO_2 and QC lasers. In the QC laser, the wavelength is selected by the grating, and the power is controlled by the input current and cavity temperature without directly controlling the cavity length. This control system likely changed the wavelength with the gain curve of the laser. The results of the benchtop experiments showed that the gap in the path difference between the probe and local path lengths, $\Delta(\delta L)$ must be close to zero to improve the mechanical vibration compensation of the CO_2/QC laser interferometer.

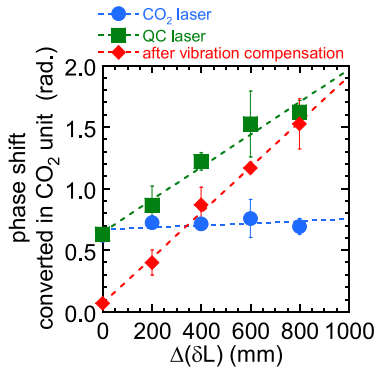

Fig. 6 Relation between $\Delta(\delta L)$ and the peak-to-peak phase shift. δL_p and δL_r are fixed to be 116 mm.

4. Optical Design in LHD

Figure 7 illustrates the overall view of the CO_2/QC laser-imaging interferometer in LHD. To suppress mechanical vibration, all optical components of the CO_2/QC laser imaging interferometer were located on a vibration-protected stand with a pneumatic spring. In LHD, the CO_2 and QC lasers are located at the bottom of the vibration-protected stand on the underground floor of the LHD building, as shown in Fig. 7. The local and probe beams were transmitted through the plasma from the bottom to the top and subsequently detected by the system on the top of the vibration-protected stand. The previous CO_2/YAG laser-imaging interferometer used two-sheet probe beams. However, as illustrated in Fig. 7, new CO_2/QC laser imaging interferometer uses three sheet probe beams to cover almost the entire plasma cross-section.

Figure 8 shows details of the optical system in the transmission section. The CO_2 laser (Access Laser Corporation, model Merit-S) exhibited an output power of 8 W. The wavelength was fixed at 10.6 μm, and the output power was stabilized by controlling the temperature of the cavity to suppress thermal expansion and to control the cavity length with feedback control using a piezoelectric component. The QC laser (Pranalytica Inc., model 1101-46-CW-700-EGC-TT) had an output power of 700 mW. The wavelength was fixed at 4.6 μm using a thermoelectric cooler. A selection of 4.6 μm instead of 5.26 μm was performed for the benchtop experiments to avoid water vapor absorption. In addition, a higher-power QC laser is an effective countermeasure against low window transmittance and low detector sensitivity. Both CO_2 and QC lasers are water-cooling types to suppress mechanical vibrations. The BS splits the outgoing beams from the CO_2 and QC lasers into local and probe beams, as shown in Fig. 8. The frequency shifts were the same as those in the benchtop experiment listed in Table 1 for the local and probe beams. Next, the CO_2 and QC laser beams were aligned coaxially by the BC. In Fig. 8, the red and blue lines represent probe and local beams after combining, respectively. The local and probe beams were collimated using spherical mirrors ($f = 750$ mm and $f = 250$ mm) on the first floor and moved to the second floor. The probe beam was split into three beams and expanded in the y-direction using

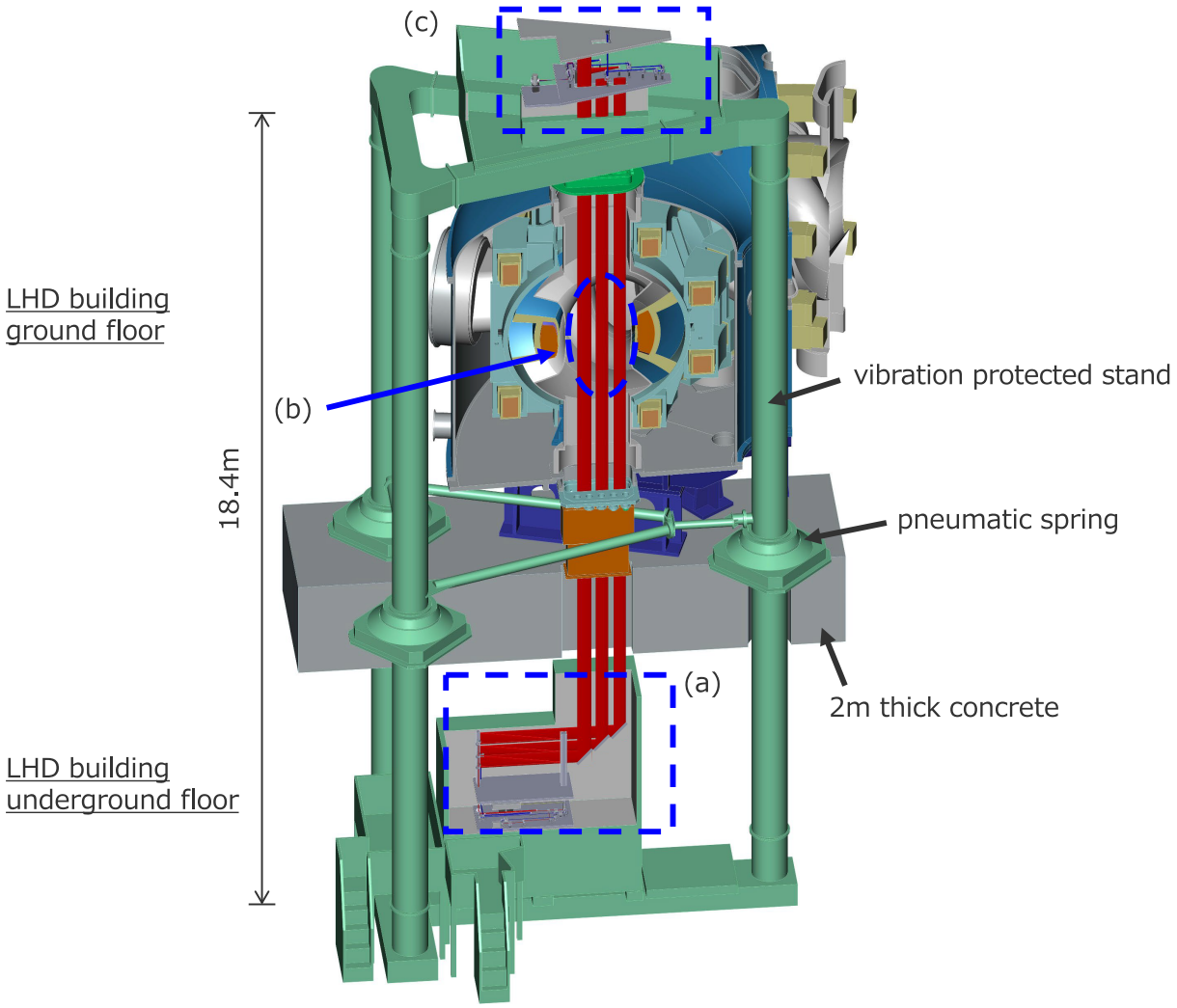

Fig. 7 Overall view of the CO_2/QC laser imaging interferometer system in LHD. Details of the (a) transmission, (b) plasma, and (c) detection sections surrounded by blue-dashed line, as shown in Figs. 8, 10 and 11. The optical path length from the laser aperture to the detector was ~ 30 m.

three pairs of cylindrical mirrors (from top $f = 1516$ mm and $f = -71.5$ mm, $f = 1516$ mm and $f = -71.5$ mm, $f = 1750$ mm and $f = -71.5$ mm) on the second floor. The three-sheet probe beams and narrow local beam were injected into the plasma passing through a window of the LHD vacuum vessel. The windows were made of ZnSe and had an effective size of 280×50 mm and a thickness of 15 mm. An indium alloy was used as a vacuum seal.

Figure 9 shows the profiles of the three-sheet probe beams measured at the measurement positions in Fig. 8. Here, probe beams (a-1)(a-2), (b-1)(b-2), and (c-1)(c-2) correspond to the top, middle, and bottom beams in Fig. 8, respectively. The beam widths in the y-direction of the three probes (a-2), (b-2), (c-2), and the local beam (d-2) were identical and equal to 280, 240, 250, and 40 mm, respectively. Three sheet probe beams of the CO_2 and QC lasers were overexpanded, and the edge was trimmed using cylindrical mirrors to obtain a sufficiently strong signal at the beam edge. The higher beam power of the QC laser compared with that of the CO_2 laser compensates for the lower transmissivity of the pair of vacuum windows (100% and 16% for the CO_2 and QC lasers, respectively) and lower sensitivity of the MCT for the QC laser compared with the CO_2 laser, as shown in Fig. 4 (a). In Fig. 9, the probe beams, (a-2), (b-2), and (c-2) correspond to the inner, center, and outer beams in Fig. 10, respectively. This measurement cross-section is called the inward-shifted configuration, in which the magnetic axis position R_{ax} is 3.6 m. The cross-section was 1.825 deg. away from the vertically elongated cross-section; thus, the flux surface was slightly tilted. The red and blue hatched regions represent the line-of-sight of the sheet probe and local beams, respectively. The three-sheet probe beams covered almost the entire plasma region, including the plasma boundaries. Because the beat signal is unstable at both ends of each probe beam, approximately 60 of the 80 channels can be used for analysis in practice. Channels outside the plasma are indispensable for evaluating

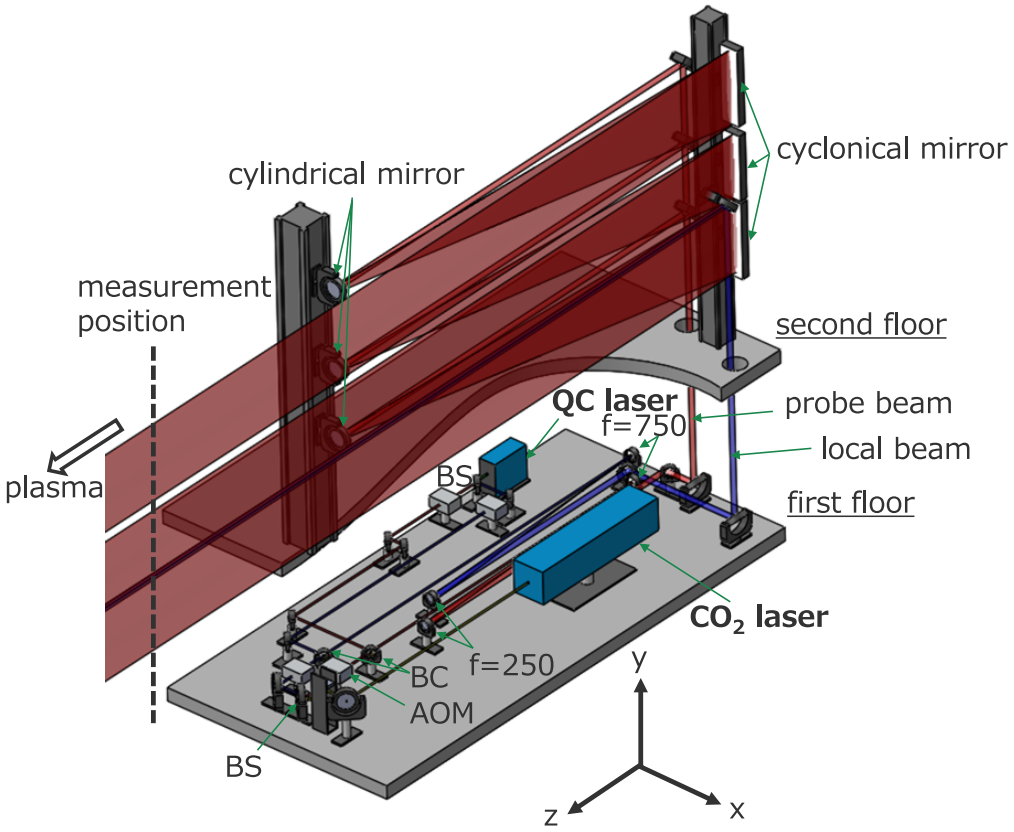

Fig. 8 Details of the optical system in the transmission section located at the underground floor of the LHD building.

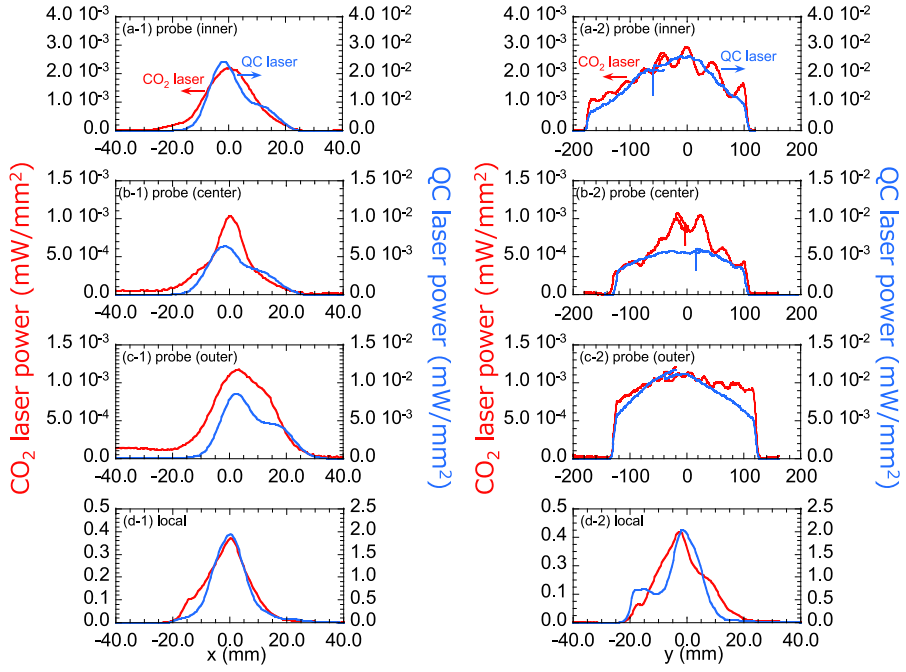

Fig. 9 Beam profiles of three sheet probe and local beams in x- and y-directions.

the electron density profile because the local beam passes through the inside of the plasma. In the initial version of the CO_2/YAG laser interferometer system, the local beam passed outside the plasma in the outer port. In the CO_2/QC laser interferometer system, a local beam was set in the middle port to precisely measure the plasma boundary. A strong phase change in the local beam can affect the phase measurement. However, a comparison with pellet ablation

measurements using an FIR interferometer, where the local beam passed outside the plasma, confirmed that this effect was negligible. In addition, the direct measurement of the boundary position where the electron density becomes zero plays an important role in determining the boundary conditions for Abel inversion to evaluate the flux surface-averaged radial density profiles. After passing through the plasma, the local and probe beams were detected at the optical system on top of the vibration-protected stand, as shown in area (c) of Fig. 7. The CO_2/QC laser imaging interferometer uses the sheet-beam imaging method, and the optical detection system is designed to form an image on the equatorial plane (Z = 0 m in Fig. 10) using a combination of parabolic mirrors and lenses.

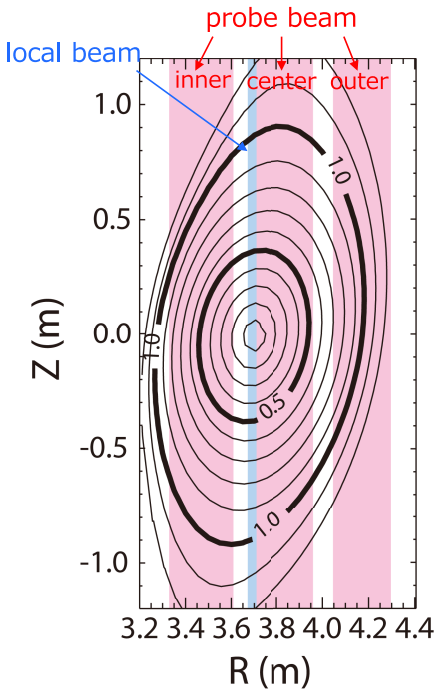

Fig. 10 Measurement cross-section of the inward shifted configuration.

The detailed layout of the detection optics of the outer beam is illustrated in Fig. 11. Similar optical systems were installed for both the central and inner beams. The channel numbers were 32 for the inner and outer beams and 16 for the center beam obtained using multichannel MCT detector arrays developed by the Infrared Systems Development Corporation. The 0.5 mm × 0.5 mm elements were vertically aligned at 0.12 mm intervals. The focal length of the parabolic mirrors, lenses, number of MCT detector channels, channel spacing in the plasma, and demagnification for the detection of the three probe beams are summarized in Table 2. The focal depth of imaging optics can be defined by a quarter Talbot length, where the phase grating at the object plane changes to an intensity grating [23]. The quarter Talbot length is defined as $Z_{qT} = a^2/2\lambda$, where a is the period of the phase grating and λ is the wavelength of

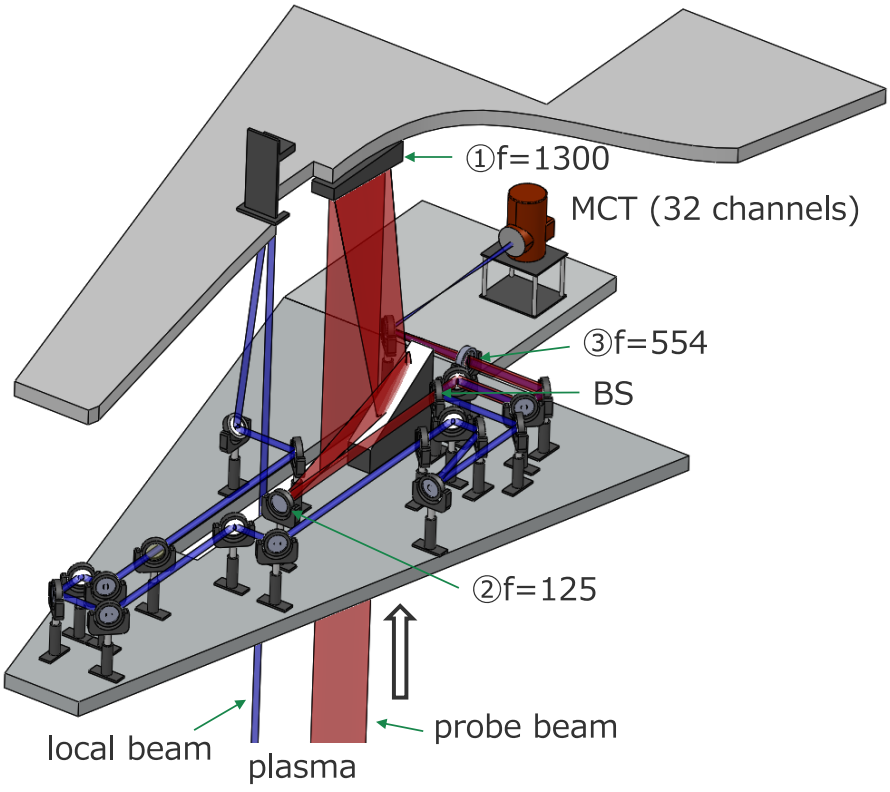

Fig. 11 Optical system of the detection part for the CO_2/QC laser imaging interferometer in LHD (outer line of sight). Red and blue lines indicate the probe and local beam, respectively.

the light source. The smallest values for the lowest a were twice the channel spacing in the plasma, which is the maximum measurable period determined by the sampling theorem, and the values were 20, 26, and 24 mm for the outer, central, and inner beams, respectively. Z_{qT} values for the three beams were 18.9, 31.9, and 27.2 m. These were significantly longer than the plasma size, which was $\sim \pm 1$ m for Z = 0 m. Thus, the imaging condition was satisfied for all the objects in the plasma. The optical systems were also carefully designed to minimize the uncompensated vibration components due to the frequency drift of the QC laser, as discussed in Sec. 3. The probe path length was designed to satisfy the imaging condition, and the local path length was adjusted to equalize the path difference between the probe and locals of the three beams, which is $\Delta(\delta L) = 0$ in Sec. 3. The probe and local beams interfere via the BS and mixed heterodyne beat signals of 190 and 100 kHz for the CO_2 and QC lasers, detected by the 32 channel MCT detector array. The MCT detector and its amplifiers were shielded by a 10 cm-thick boron-added polyethylene shield box to avoid damage by neutrons. In addition, 10 mm-thick lead plates were placed above and below the shield box to dampen gamma rays. The detector output signals were transmitted to the acquisition room outside the LHD torus hall using BNC cables. A compact PCI (National Instruments, PXI-1042) was used to directly acquire the beat signal for five seconds at a sampling rate of 1 MHz. The time evolution of the phase shift was calculated using a digital phase demodulation technique [13, 14, 22] and the time evolution of the line-integrated electron density was measured. A single-channel analog phase counter [24] with vibration compensation was developed for real-time monitoring and long-term discharge.

Table 2 Optical components and detectors for imaging detection at each line of sight.

	optical component			MCT detector		
	①	②	③	number of channels	channel spacing in plasma	demagnification
outer	off-axis parabolic mirror f=1300	paraboli c mirror f=125	ZnSe lens f=554	32	10mm	1/16.1
center	off-axis parabolic mirror f=1015	ZnSe lens f=127	ZnSe lens f=254	16	13mm	1/21
inner	off-axis parabolic mirror f=1315	paraboli c mirror f=125	ZnSe lens f=504	32	12mm	1/19.4

5. Measurement Results in LHD

5.1 Results of vibration compensation

Instead of the CO_2/YAG laser imaging interferometer, the operation of the CO_2/QC laser imaging interferometer started with the 22nd LHD experimental campaign in 2020. Figure 12 shows the measurement results for the line-of-sight at $R = 3.75$ m. Plasma is a gas-fueled discharge with electron cyclotron resonant heating (ECRH). Fig. 12 (a) shows the time evolution of the phase shift of the CO_2 and QC laser interferometers. As shown in Fig. 12 (a), a contribution of the electron density is larger in the CO_2 laser interferometer and that of the mechanical vibration is larger in the QC laser interferometer. This difference is owing to the positive and negative proportionality of the laser wavelength to the electron density and mechanical vibration, respectively, as shown in Eq. (1). Fig. 12 (b) shows the line-integrated density and mechanical vibration, which are obtained from Eq. (2) and (3). The mechanical vibrations were converted into a unit of line-integrated density. As shown in Fig. 12 (b), the line-integrated density and mechanical vibrations were clearly separated. Fig-

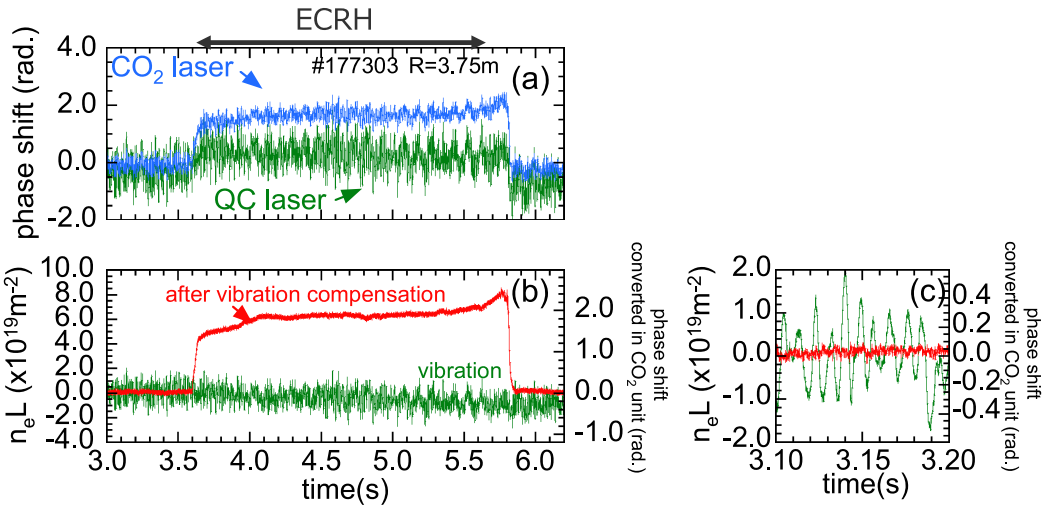

Fig. 12 Time evolution of (a) the phase shifts of the CO_2 and QC lasers, (b) line-integrated electron density and vibration component, and (c) its expanded view at $t = 3.1$ - 3.2 s before plasma production. Magnetic axis position R_{ax} is 3.6 m at $B_t = 2.85$ T (inward shifted configuration). Shot number: #177303.

ure 12 (c) shows an expanded view of the evolution of the phase shift before plasma production at t = 3.1 - 3.2 s. The peak-to-peak values of the original mechanical vibration were 4×10^{19} m^{-2}, corresponding to ~1.19 rad. in units of the CO_2 laser wavelength. The CO_2/QC laser imaging interferometer successfully compensated for the vibration to 5.03×10^{18} m^{-2}, which corresponds to ~0.15 rad. in units of the CO_2 laser wavelength. This residual uncompensated vibration component corresponds to 2.80×10^{18} m^{-3} of the line-averaged density for a path length of L = 1.8 m. The root mean square was 0.03 rad, corresponding to 1.0×10^{18} m^{-2} and 0.56×10^{18} m^{-3} for the line-integrated and line-averaged densities, respectively. Thus, even in low-density experiments in LHD, where the line-averaged density was approximately 1.0×10^{19} m^{-3}, the CO_2/QC laser interferometer provided data with reasonably good accuracy. Unfortunately, the uncompensated component of the CO_2/QC laser interferometer in LHD was 3.75 times larger than that in the benchtop experiment. We tested the Pranalytica QC laser on the benchtop, and the residual vibration component was almost the same as that in the benchtop experiments using the Hamamatsu QC laser. Therefore, the residual components are likely caused by the coaxial alignment accuracy and the difference in the wavefront distortion between the CO_2 and QC lasers. This is likely because the optical path length is much longer than in the benchtop experiment, requiring more precise coaxial adjustment, and because some optics, such as beam splitters and windows, are not optimized for the QC laser wavelength of 4.6 μm. The measurement accuracy of the CO_2/QC laser interferometer in LHD was comparable to that of the best-performing channel of the previous CO_2/YAG laser interferometer with the same optical system and analysis [12]. Most importantly, in the CO_2/YAG laser interferometer, such good measurement accuracy was limited to a few channels; however, for the CO_2/QC laser interferometer, a desirable compensation accuracy could be obtained for all channels. This result demonstrates the first high-temperature plasma density measurement using a two-color laser interferometer with CO_2 and QC lasers.

5.2 Evaluation of the radial density profile

5.2.1 Radial density profiles in gas-fueled plasma

In this section, an example of the evaluated radial density profiles in gas-fueled plasma is presented. To evaluate the radial density profiles, we used the Abel inversion with an optimized regularization parameter using GCV [2,25,26]. Compared with FIR laser interferometers, which apply the same optimized Abel inversion [2], the CO_2/QC laser interferometer has a fine spatial resolution and does not require interpolation between channels [12]. In this schema, the flux surface is determined by the interpolation of a pre-calculated equilibrium database [27]. The flux surface was determined based on the conditions under which the electron temperature profiles inside and outside the magnetic axis coincide [27].

Figure 13 shows the radial profile of the electron temperature and electron density and a comparison of the measured and calculated line-integrated density profiles. The magnetic configuration was an inward-shifted configuration, in which the magnetic axis position was 3.6 m. As shown in Fig. 13 (a), the electron temperature profiles inside and outside the magnetic axis agreed, indicating that the determined equilibrium accounts for the measured temperature profiles. The normalized radius ρ is defined as the effective minor radius normalized by radius a99, where the electron pressure inside a99 is 99% of the total electron pressure [27]. Fig. 13 (b) shows the radial electron density profiles measured using the CO_2/QC laser and FIR laser interferometers and YAG Thomson scattering [6]. The red symbols and black dashed lines indicate the CO_2/QC laser imaging and FIR laser interferometers evaluated by Abel inversion, respectively. The green and blue symbols indicate the internal and external profiles, respectively, as measured using Thomson scattering. The absolute value of the Thomson density profile was determined by fitting the line-integrated Thomson density profile to the line-integrated density measured using an FIR laser interferometer. As shown in Fig. 13 (b), three profiles were within the uncertainty of the Thomson density profiles. The CO_2/QC laser

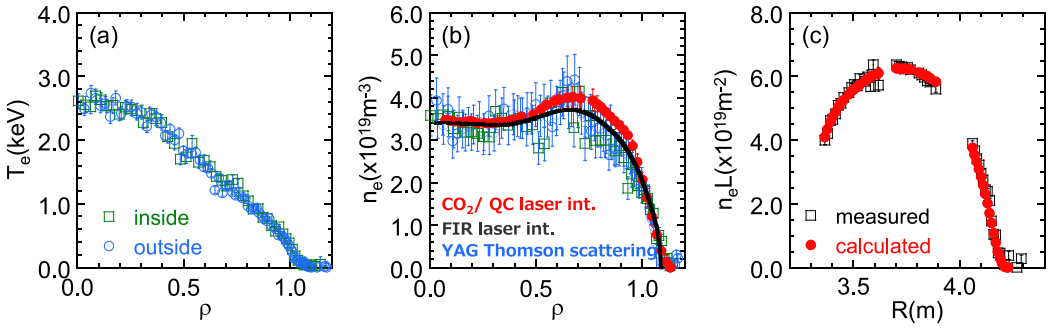

Fig. 13 Normalized minor radius profiles of the (a) electron temperature and (b) density and major radius profile of (c) line-integrated electron density for inward-shifted configuration (R_{ax} = 3.6 m). Shot number: #177297.

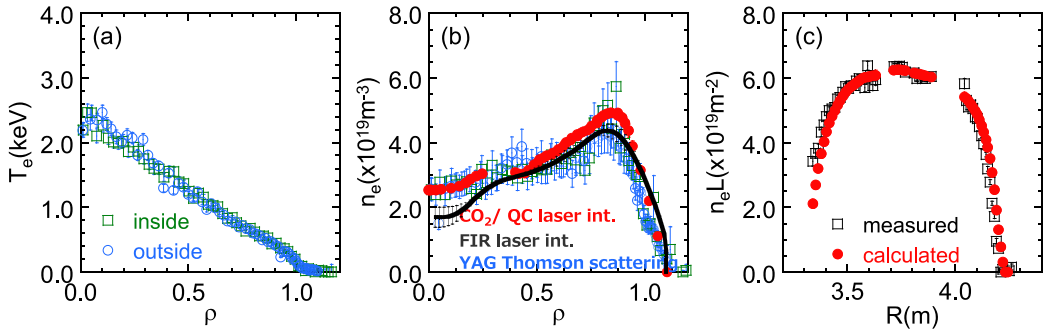

Fig. 14 Normalized minor radius profiles of (a) the electron temperature and (b) density and major radius profile of (c) line-integrated electron density for outward-shifted configuration (R_{ax} = 3.8 m). Shot number: #177356.

imaging interferometer shows a hollower-density profile and a higher peak density at $\rho = 0.8$ than the density profile of the FIR laser interferometer. The line-integrated density profile is more accurately measured with a fine spatial resolution using the CO_2/QC laser interferometer than with the FIR interferometer; thus, the profile of the CO_2/QC laser interferometer must be more reliable. Figure 13 (c) shows the measured and calculated line-integrated density profile, which is the line integration of the radial density profile along the measurement chords. These values agreed , indicating that the Abel inversion was numerically justified.

Figure 14 shows another example measured in an outward-shifted configuration, where the magnetic axis position was 3.8 m. As shown in Fig. 14 (a), electron temperature profiles inside and outside the magnetic axis agree, indicating that the flux surface is correctly determined. As shown in Fig. 14 (b), the electron density profiles are hollower than the inward shifted configuration in Fig. 13 (b). A sharp density peak at $\rho = 0.8$ was observed with the Thomson scattering measurement and the CO_2/QC laser imaging interferometer. Simultaneously, the FIR laser interferometer extrapolates the chords in the edge region and overestimates the density at ρ >1.0, resulting in an underestimation of the density at ρ <0.2. As shown in Fig. 14 (c), the measured and calculated line-integrated density profiles agree. These results demonstrate that the CO_2/QC laser imaging interferometer can accurately measure the density profiles using Abel inversion.

5.2.2 Radial density profile in pellet-injected super high-density plasma

The CO_2/QC laser imaging interferometer is particularly effective for pellet-fueled super high-density plasma measurements. This is because the FIR laser interferometer loses signals owing to large beam refraction. In addition, pellet injection forms a steep density gradient that requires high spatial resolution for profile measurements. Figure 15 shows the time evolution of the line-integrated electron density measured by the CO_2/QC laser imaging interferometer for the repetitive pellet-fueled plasma. In this figure, the difference in color indicates a line of sight difference. The maximum line-integrated electron density was 50×10^{19} m^{-2}, corresponding to a line-averaged density of 30×10^{19} m^{-3}. Such high-density plasma is called super-dense core (SDC) plasma [28]. In this discharge, all channels of the FIR laser interferometer lost their signals after the pellet injection. However, the CO_2/QC laser interferometer operated without phase jumping. After the last pellet was injected, the density started to decay gradually, and at t = 4.6 s, the density around the central region suddenly decreased, but increased in the outer region, indicating that it was pumped from the central to the outer region. The behavior before and after this event is shown in the expanded figure. This collapse is called the core density collapse (CDC). This event occurs owing to the growth of ballooning instability, which is driven by an increase in the pressure gradient at the low-field side [29]. The phase variations at the pellet injection and CDC events corresponded to 2 and 1.1 kHz, respectively. Because the BPF width is set to ±5 kHz for this analysis, the CO_2/QC laser imaging interferometer can measure the instantaneous profile changes that occur in high-density plasma.

Figure 16 shows the electron density profile before and after the CDC event from Thomson scattering and CO_2/QC laser-imaging interferometer. The magnetic flux surface is determined by matching the electron pressure profiles inside and outside the magnetic axis. This is because the electron temperature profile cannot be used to determine the appropriate flux surface because the electron temperature is flat and is insensitive to different flux surfaces with different beta values. As shown in Fig. 16 (a-1) and (b-1), the electron pressure profiles are used, instead of the electron temperature profile. As shown in Fig. 16 (a-2) and (b-2), the density profiles from both diagnostics show similar behaviors before and after CDC. The steep density gradient at ρ = 0.3 - 0.5 before the CDC flattened after the event. The density at ρ >0.5 increases after the CDC because it is pumped from the core region at ρ <0.5. After pellet injection, the electron temperature was flat in the core region; thus, the steep density gradient at ρ = 0.3 - 0.5 before the CDC determined the stability limit of the bal-

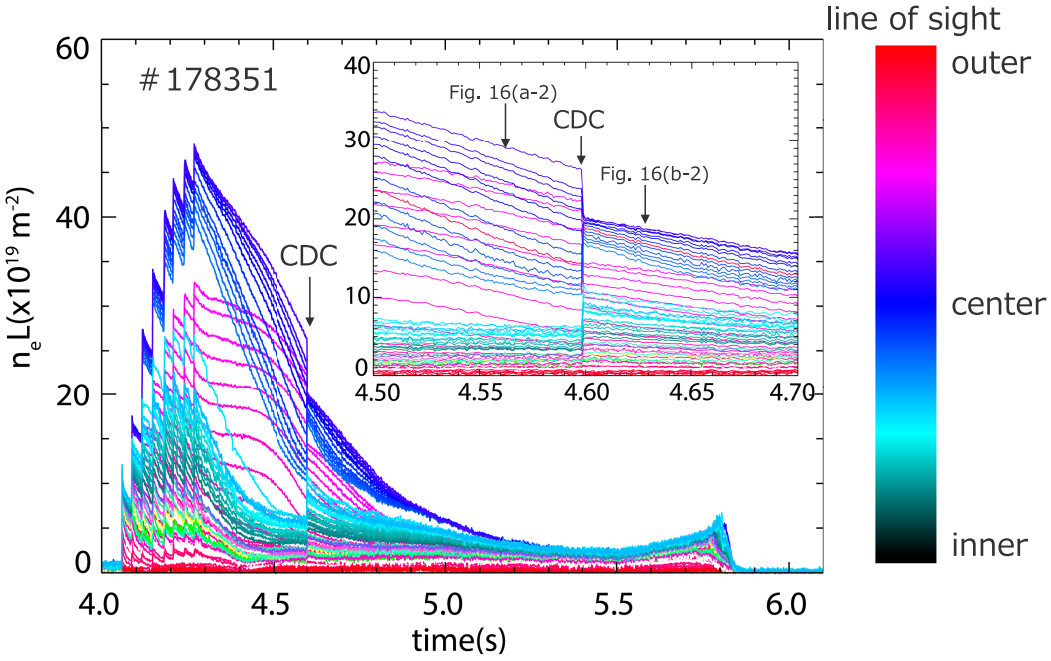

Fig. 15 Time evolution of line-integrated electron density in high density pellet-fueled plasma and its expanded view at t = 4.50 - 4.70 s when CDC occurred. Magnetic axis position R_{ax} set as 3.85 m and toroidal magnetic field strength B_t set as −2.571 T on the magnetic axis. Shot number: #178351.

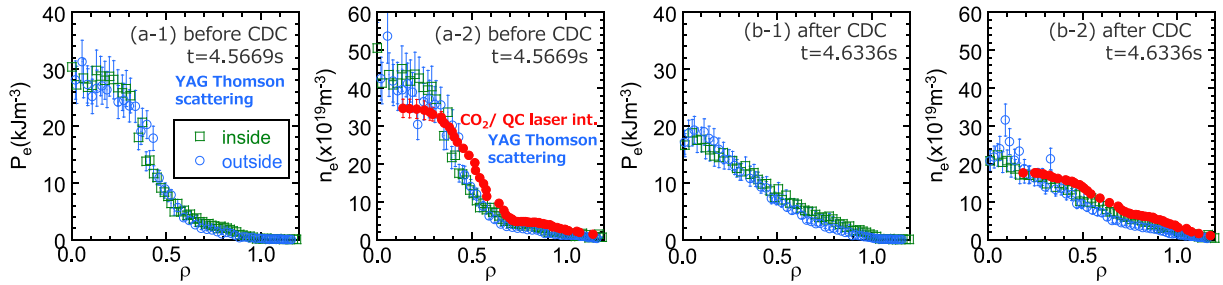

Fig. 16 Normalized minor radius profiles of (a-1)(b-1) the electron pressure and (a-2)(b-2) density (a-1)(a-2) before (t = 4.5669 s) and (b-1)(b-2) after CDC (t = 4.6336 s). Symbol color is the same as Figs. 13 (a) and (b). Shot number: #178351.

looning mode. There were discrepancies between the density profiles obtained with Thomson scattering measurements and those obtained with the CO_2/QC laser imaging interferometer. The lack of data points at ρ <0.2 in the density profile from the CO_2/QC laser imaging interferometer is because there is a magnetic axis in the dead space between the center and outer sheet beams. To determine the Thomson density profiles, we used calibration factors obtained from nitrogen gas Raman scattering. The discrepancies in the density profiles obtained with Thomson scattering measurements and the CO_2/QC laser imaging interferometer were larger than those in the gas-fueled cases, as described in the previous section. These discrepancies were partly owing to the uncertainty of the calibration factor of the Thomson density measurements and uncertainty in determining the flux surface. Abel inversion is numerically easier with peak-density profiles. Thus, if the flux surface is measured using the CO_2/QC laser interferometer to select only the minimum mean square error, a better inversion can be obtained. This is the next step of this investigation.

5.3 Measurement of the macro-scale density fluctuation before radiation collapse

The CO_2/QC laser imaging interferometer is also advantageous for the measurement of macro-scale electron density fluctuations. Macro-scale density fluctuations were observed before the radiation collapse during long-term discharge. In other words, macro-scale density fluctuation is a precursor to radiation collapse. The fine spatial structure of the precursor signal was measured using the features of the CO_2/QC laser imaging interferometer. Because the duration of the data acquisition was limited to 5 s, the density of the long-term discharge was monitored using an analog phase counter. The detailed spatial struc-

ture of the macro-scale precursor was determined using an event trigger. Figure 17 (a) shows the time evolution of the line-integrated electron density calculated using the single-channel analog phase counter of the CO_2/QC laser imaging interferometer. The timing of radiation collapse was determined from the threshold of the bolometer signal [30, 31], as shown in Fig. 17 (b). Subsequently, the CO_2/QC laser imaging interferometer was acquired from t = 25.072 s with 1 MHz sampling for five seconds. Figure 18 (a) shows the time evolution of the line-integrated electron density measured by the CO_2/QC laser imaging interferometer immediately before the plasma collapse at R = 3.75 m. As shown in Fig. 18 (a), the fluctuation appeared from t = 25.25 s, and its amplitude increased in time, and the plasma collapsed at t = 25.32 s. This result indicates that the growth of macro-scale instability induces an increase in radiation and terminates the plasma. Figure 18 (b) is an expanded view of the fluctuation component, and Fig. 18 (c) illustrates the time evolution of the

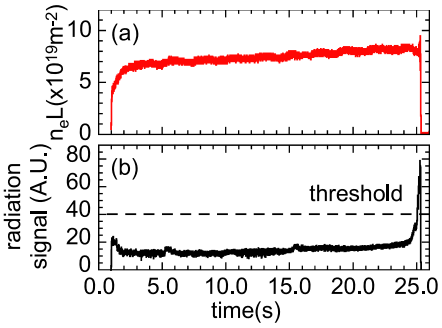

Fig. 17 Time evolution of line-integrated (a) electron density and (b) radiation signal in long-term discharge. Magnetic axis position R_{ax} set as 3.6 m and toroidal magnetic field strength B_t set to 2.750 T on the magnetic axis. Shot number: #179225.

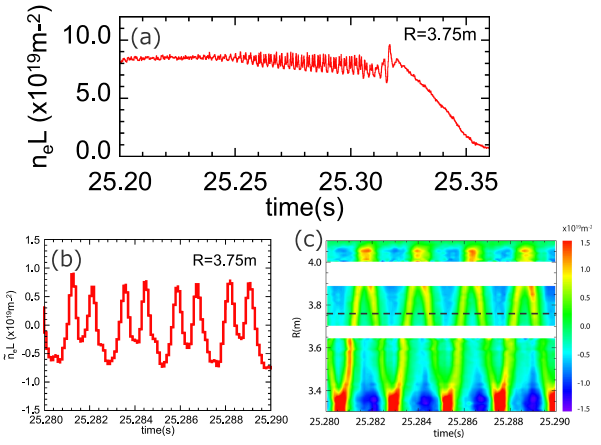

Fig. 18 Time evolution of (a) line-integrated electron density just before radiation collapse, (b) macro-scale fluctuation amplitude, and (c) contour plot of macro-scale fluctuation amplitude at t = 25.28 - 25.29 s.

macro-scale instability profile at t = 25.28 - 25.29 s. The observed fluctuations, as shown in Fig. 18 (b) correspond to the position of the dashed line in Fig. 18 (c). The turbulence amplitude was larger at the edge region, indicating that there were macro-scale fluctuations at the edge region and rotated in the poloidal direction at 400 Hz. The CO_2/QC laser imaging interferometer enabled the measurement of long-term discharges owing to its improved measurement stability, and its high spatial and temporal resolution was sufficient to measure the behavior of the macro-scale fluctuation profiles.

6. Summary

A two-color CO_2/QC laser imaging interferometer was developed for stable and reliable measurements of electron density with fine spatial and temporal resolutions in LHD. A CO_2 laser was selected as the light source to prevent phase jumping owing to beam refraction, and a QC laser was selected because of its compactness and high power to compensate for mechanical vibrations. The developed two-color CO_2/QC laser interferometer utilizes the novel concept of a detection system in which two wavelengths are detected by a single detector and separated using a different heterodyne beat frequency. This detection system has simpler optics and improves the accuracy of vibration compensation. The benchtop experiment revealed that the coherent lengths of both the CO_2 and QC lasers were sufficient, and the output wavelength of the CO_2 laser was sufficiently stable. The wavelength of the QC laser changed over time. We demonstrated that the effect of the unstable wavelength can be reduced by minimizing the gap in the path difference of the probe and local path lengths of the two detectors. Consequently, in the benchtop experiments, the effect of mechanical vibration could be reduced to 1.34×10^{18} m^{-2}, attaining a measurement accuracy that is four times that of the conventional CO_2/YAG laser interferometer in LHD. After the benchtop experiments, we installed a CO_2/QC two-color laser imaging interferometer in LHD. In LHD, imaging optics were employed to achieve a high spatial resolution, and three sheet beams covered almost the entire region of the plasma cross-section. Owing to the mechanical vibration compensation, the effect of mechanical vibration can be reduced to 5.03×10^{18} m^{-2}. Unfortunately, the uncompensated component of the CO_2/QC laser interferometer in LHD was 3.75 times larger than that in the benchtop experiment. The deterioration of the uncompensated components compared to the benchtop experiments was likely due to the coaxial alignment accuracy and distortion of the wavefront from the unoptimized window and beam splitters. In some cases, we could reduce the residual components to 3.0×10^{18} m^{-2} using a high-precision coaxial alignment. The uncompensated components were comparable to the best value of the CO_2/YAG interferometer. However, in the CO_2/YAG laser interferometer, the mea-

surement accuracy was limited to a few channels, and for the CO_2/QC laser interferometer, good compensation accuracy could be obtained for all channels. In addition, the stability of the heterodyne beat signal was much better in the CO_2/QC laser interferometer than in the CO_2/YAG laser interferometer. The large number of channels enabled the evaluation of fine radial density profiles using Abel inversion with the least-squares method and an optimized regularization technique. Hollowed density profiles in the gas-fueled discharge and peaked density profiles in the pellet-injected discharge were obtained with good accuracy and in agreement with Thomson scattering. In the pellet-injected plasma, all the channels worked without phase jumping at a line-averaged density of 30×10^{19} m^{-3}. In addition, a large number of channels enabled measurements of the fine structures of macro-scale fluctuations, which was the precursor of the radiation collapse of long-term discharge. The density of the long-term discharge was monitored by applying an analog phase counter to the channel close to the plasma center. This output was obtained in real-time and could be used as a source of density feedback control in the next step. These measurement results of gas-fueled plasma, pellet-injected plasma, and macro-scale instability are the first results of high-temperature plasma measurements using a CO_2/QC two-color laser imaging interferometer and provide important insights into the development of two-color laser interferometers in future fusion devices.

7. Discussion

Finally, a comparison of the CO_2/QC laser interferometer with dispersion interferometers and polarimeters is discussed. These two diagnostics and the two-color interferometer are candidates for electron density diagnostics in ITER and future reactors. Both the dispersion interferometer and polarimeter were installed in the LHD, and systems that incorporate them have worked in previous LHD hydrogen campaigns [32, 33]. The dispersion interferometer uses one laser and generates a second-harmonic wave using a nonlinear crystal [32, 34, 35]. The dispersion interferometer does not require the optical-axis alignment of two different wavelengths, it does not depend on the laser conditions, does not have phase jumps, and does not require a reference channel to pass outside the plasma. The dispersion interferometer presently works in W7-X [35] and is planned for use in ITER [36, 37]. The noise level of the CO_2 laser dispersion interferometer in LHD was 1.3×10^{18} m^{-2} for the peak-to-peak value at 10 kHz sampling. This peak-to-peak value is five times the residual vibration component of the CO_2/QC laser interferometer. However, a multichannel system is difficult to realize with the dispersion interferometer because of the low generation efficiency of the second-harmonic wave.

The use of a polarimeter to measure the Faraday rotation is another technique for obtaining density measurements. The Faraday rotation angle is a cross-product line integral of the electron density and magnetic field parallel to the laser beam axis. Historically, a polarimeter combined with an interferometer was developed to measure the internal magnetic fields [5]. However, a polarimeter has also been proposed to measure electron density under a known magnetic field [38]. The advantage of the Faraday rotation polarimeter is that it does not have phase jumps and its measurements are not affected by mechanical vibrations. In addition, a reference channel that passes outside the plasma is not required. The noise level of the CO_2 laser Faraday rotation polarimeter in LHD was 0.01 deg., corresponding to 2.8×10^{18} m^{-2}, which is also 1.5 times the CO_2/QC laser interferometer. An essential advantage of dispersion interferometers and polarimeters is that, in principle, a phase jump does not occur. This is a significant advantage in achieving stable and reliable density monitoring. In contrast, phase jumps have never occurred even with the CO_2/QC laser imaging interferometer in LHD. A central density of 30×10^{19} m^{-3} is high, even in future reactor operations. Thus, it is likely that the phase jump owing to beam refraction will not be a problem in the CO_2/QC laser interferometer in future reactors. However, the system of the CO_2/QC laser interferometer in LHD is entirely located on a vibration-protected stand. If optics are in the vacuum chamber, strong external vibrations, such as the disruption of a tokamak, may cause signal loss. In this case, an active beam-control system is required [19]. The interferometer has a better chord spatial resolution than the dispersion interferometer and polarimeter. Even in a multi-beam system, where one beam corresponds to one measurement channel, an optical system, in particular a detection system, is much simpler and it is easier to increase its number of channels. Additionally, QC lasers are valuable for future applications. A QC laser is currently under development, and a wavelength of approximately 10 μm with an output power of 1 W will be commercially available in the near future. The present CO_2 laser is powerful and stable; however, its wavelength feedback control occasionally becomes uncontrollable and requires tuning. In addition, the annual maintenance of the cavity mirrors is necessary for good performance. However, QC lasers do not require tuning and maintenance. This is a significant advantage for a reliable interferometer. The CO_2/QC laser imaging interferometer system was optimized for LHD. However, the results obtained in this development study will be valuable for two-color interferometers in future devices.

Acknowledgments

LHD data can be accessed from the LHD data repository `https://www-lhd.nifs.ac.jp/pub/Repository_en.html`. The authors would like to thank Dr. Andrew Duran of Infrared Systems Development Corporation for providing us responsivity data of MCT detector and Dr. Kumar Patel of Pranalytica corporation for

the fruitful discussion on the QC laser. The authors thank Dr. C. Suzuki for providing the magnetic database, which is essential for Abel inversion. The authors would like to thank Dr. M. Kobayashi and Dr. K. Mukai for providing the bolometer data and Dr. Y. Yoshimura for operating the long-term discharge using an event trigger. The authors thank the LHD experiment group for their excellent work on the operation of LHD. This work was supported by NIFS Grants (17ULHH013, 18ULHH013, 19ULHH013, 20ULHH013, 21ULHH013, and 22ULHH013) and JSPS grants (21J12314, 16H04620, and 21H04458).

[1] K. Tanaka *et al.*, Fusion Sci. Technol. **58**, 70 (2010).
[2] Y. Ohtani *et al.*, Plasma Phys. Control. Fusion **62**, 025029 (2020).
[3] K. Watanabe *et al.*, Phys. Plasmas **18**, 056119 (2011).
[4] C. Michael *et al.*, Plasma Fusion Res. **3**, S1071 (2008).
[5] D. Veron, Infrared Millimeter Waves **2**, 67 (1979).
[6] I. Yamada *et al.*, Fusion Sci. Technol. **58**, 345 (2010).
[7] K. Kawahata, K. Tanaka, Y. Ito, A. Ejiri and R. Wylde, Rev. Sci. Instrum. **70**, 695 (1999).
[8] K. Kawahata, K. Tanaka, Y. Ito, A. Ejiri and S. Okajima, Rev. Sci. Instrum. **70**, 707 (1999).
[9] K. Kawahata, A. Ejiri, K. Tanaka, Y. Ito and S. Okajima, Fusion Eng. Des. **34**, 393 (1997).
[10] K. Tanaka *et al.*, Plasma Fusion Res. **3**, 050 (2008).
[11] T. Akiyama *et al.*, Fusion Sci. Technol. **58**, 352 (2010).
[12] K. Tanaka *et al.*, Rev. Sci. Instrum. **75**, 3429 (2004).
[13] H. Sakai *et al.*, Plasma Fusion Res. (submitted).
[14] K. Tanaka *et al.*, Plasma Fusion Res. **2**, S1033 (2007).
[15] K. Tanaka, L. Vyacheslavov, K. Kawahata, T. Tokuzawa and S. Okajima, Rev. Sci. Instrum. **72**, 1089 (2001).
[16] T. Carlstrom, D. Ahlgren and J. Crosbie, Rev. Sci. Instrum. **59**, 1063 (1988).
[17] J. Irby, E. Marmar, E. Sevillano and S. Wolfe, Rev. Sci. Instrum. **59**, 1568 (1988).
[18] Y. Kawano, A. Nagashima, T. Hatae and S. Gunji, Rev. Sci. Instrum. **67**, 1520 (1996).
[19] M. Van Zeeland *et al.*, Plasma Phys. Control. Fusion **59**, 125005 (2017).
[20] H. Sasao *et al.*, J. Instrum. **11**, C02082 (2016).
[21] K. Kawahata *et al.*, Rev. Sci. Instrum. **77**, 10F132 (2006).
[22] Y. Jiang, D. Brower, L. Zeng and J. Howard, Rev. Sci. Instrum. **68**, 902 (1997).
[23] L. Rayleigh, The London, Edinburgh, and Dublin Philosophical Magazine and Journal of Science **11**, 196 (1881).
[24] Y. Ito, K. Haba, T. Tokuzawa and K. Kawahata, Fusion Eng. Des. **56**, 965 (2001).
[25] M. Anton *et al.*, Plasma Phys. Control. Fusion **38**, 1849 (1996).
[26] N. Shi *et al.*, Rev. Sci. Instrum. **85**, 053506 (2014).
[27] C. Suzuki *et al.*, Plasma Phys. Control. Fusion **55**, 014016 (2012).
[28] N. Ohyabu *et al.*, Phys. Rev. Lett. **97**, 055002 (2006).
[29] S. Ohdachi *et al.*, Nucl. Fusion **57**, 066042 (2017).
[30] B. Peterson *et al.*, Fusion Sci. Technol. **58**, 412 (2010).
[31] K. Mukai, B.J. Peterson, S.N. Pandya, R. Sano and M. Itomi, Plasma Fusion Res. **9**, 3402037 (2014).
[32] T. Akiyama, R. Yasuhara, K. Kawahata, S. Okajima and K. Nakayama, Rev. Sci. Instrum. **85**, 11D301 (2014).
[33] T. Akiyama *et al.*, Rev. Sci. Instrum. **74**, 2695 (2003).
[34] P. Bagryansky *et al.*, Rev. Sci. Instrum. **77**, 053501 (2006).
[35] J. Knauer *et al.*, A new dispersion interferometer for the stellarator wendelstein 7-x, in 43rd EPS Conference on Plasma Physics, European Physical Society, 2016.
[36] T. Akiyama *et al.*, Rev. Sci. Instrum. **87**, 11E133 (2016).
[37] D.J. Campbell *et al.*, J. Fusion Energy **38**, 11 (2019).
[38] T. Kondoh *et al.*, Rev. Sci. Instrum. **75**, 3420 (2004).